Desalination and Water Treatment
www.deswater.com

doi: 10.1080/19443994.2015.1099473

57 (2016) 19301–19310
September

Taylor & Francis
Taylor & Francis Group

Effective removal of methylene blue from aqueous solution by MnO_2-modified porous $CoFe_2O_4$ microrods

Shengbiao Li, Zhigang Jia*, Zhiyu Li, Jianhong Liu

School of Chemistry and Chemical Engineering, Anhui University of Technology, No. 59 Hudong Road, Ma'anshan 243002, Anhui Province, P.R. China, Tel. +86 555 2311551; Fax: +86 555 2311882; emails: qinglanbiao@163.com (S. Li), zjchemyue@126.com (Z. Jia), 496761147@qq.com (Z. Li), liujianhong90@126.com (J. Liu)

Received 31 March 2015; Accepted 15 September 2015

ABSTRACT

MnO_2-modified porous $CoFe_2O_4$ microrods (MnO_2–CMR) were prepared by *in situ* oxidation reaction. The obtained samples were characterized by the means of scanning electron microscopy, transmission electron microscopy, X-ray diffraction, and energy dispersive spectrometer. The results showed that the $CoFe_2O_4$ microrods were successfully decorated with amorphous MnO_2. An appropriate decoration mechanism was suggested and discussed. Methylene blue (MB) was employed to evaluate the adsorption property. The measurements exhibited that the adsorption capacity was highly enhanced due to the addition of MnO_2 in the porous $CoFe_2O_4$ microrods (CMR). The adsorption capacity of the as-prepared MnO_2–CMR was investigated using a batch adsorption procedure. The kinetics and thermodynamics of the adsorption process were further investigated. The adsorption kinetics was well fitted by a pseudo-second-order model and the adsorption isotherms agree well with the Langmuir model. Thermodynamic analyses showed that MB adsorption onto the MnO_2–CMR was endothermic and spontaneous process. Furthermore, the MnO_2–CMR can be easily recycled by magnetic separation. The MnO_2–CMR developed in the present study was expected to be an efficient magnetic adsorbent for the removal of MB form wastewater.

Keywords: Nanostructures; Chemical synthesis; Water treatment; Adsorption

1. Introduction

Dyes are widely used in many industrial fields, such as paper printing, leather, and textile industries. Most of the dyes are soluble in water and some are even toxic or carcinogenic to humans. The wastewater discharged from the dye industries has a large impact on the ecological environment and human health. However, almost 10–15% of the dyes has been lost during the dyeing processes and are almost directly discharged as sullage according to the literature [1]. The migration and spreadability of these dyes with water will cause a serious environmental issue. Therefore, the efficient removal of these dyes before their discharge is very pivotal for the protection of environment.

Over the past decades, various technology, such as flocculation, coagulation, precipitation, adsorption, membrane filtration, electrochemical techniques, ozonization, sedimentation, reverse osmosis, fenton degradation, and photo degradation, etc., have been

*Corresponding author.

developed [2–10]. Among these treatment means, the adsorption technique currently seems to be the most efficient way to remove the dye effluents from the environment due to cost effectiveness, high efficiency, simple operation. Many adsorbent materials have been prepared and applied to remove the dye from the wastewater.

In recent years, magnetic materials have attracted a great deal of attention in the field of environment protection [11–13]. Compared with conventional adsorbent materials, the advantages of magnetic separation reflect in its speed, accuracy, and simplicity. Magnetic particles can be directly used as adsorbent or employed as magnetic carrier to remove contaminants from aqueous effluents [14]. The magnetic adsorbent can also be separated from the solution by a simple magnetic process once the adsorption is completed. Furthermore, the adsorbed contaminants can be stripped from the adsorbent and concentrated into a small volume for reuse of the contaminants and the magnetic adsorbent. However, magnetic nanoparticles are apt to aggregate due to high surface energy and magnetostatic interactions, which reduces their small surface areas and results in a small adsorption capacity or slow adsorption rates [15]. These disadvantages limit the applications of magnetic particles. Porous inorganic materials have high surface area and rigid texture, which is good for the materials as adsorbent or carrier. It seems to be feasible solution to make magnetic nanoparticles into porous materials for nano agglomerates.

In this work, we firstly prepared the porous cobalt ferrite microrods (CMR) and then modified CMR with amorphous manganese oxide. The *in situ* formed manganese oxides are embedded in the porous texture of cobalt ferrite microrods. The possible formation process of cobalt the ferrite/manganese oxide microrods were proposed. Furthermore, the dye adsorption capacity of the as-synthesized MnO_2−CMR for methylene blue (MB) was also investigated in details. This kind of hybrid adsorbent with easy and rapid extraction/regeneration, handy operation and non-compromised performance, may provide a better solution for the application of magnetic nanoparticles in environmental protection for water resources.

2. Experimental section

2.1. Preparation of MnO_2-modified porous $CoFe_2O_4$ microrods (MnO_2−CMR)

Porous $CoFe_2O_4$ microrods (CMR) were prepared according to the previously reported method by our group [16]. FeSO4, $H_2C_2O_4$, and $CoSO_4$ as the raw source were dissolved in the mixed solvents of ethylene glycol and water. The transparent mixture was hydrothermally treated at 120℃ for 24 h in an oven. The product was collected by centrifugation and dried in air at 100℃. The as-prepared precursor was annealed in air at 400 at the heating rate of 1℃ min^{-1}. The obtained samples were collected for further use.

To obtain MnO_2-modified porous $CoFe_2O_4$ microrods (MnO_2−CMR), 100 mg of the as-prepared CMR microrods were added into conical flask containing 50 mL of 3 M $MnSO_4$ solution and was oscillated for 2 h. Then, the soaked CMR were magnetically separated by a magnet and washed with distilled water several times. After that, 20 ml of 2 M $KMnO_4$ solution was added into conical flask and let stand for 1 h. The product was magnetically separated by a magnet, washed with distilled water several times and finally dried in an air oven at 100℃. MnO_2-modified porous $CoFe_2O_4$ microrods were denoted as MnO_2−CMR.

2.2. Characterization

The morphology of the products was characterized by a field emission scanning electron microscope (FESEM, JEOL JSM-6700F). Transmission electron microscopy (TEM) analysis was performed on a JEM 3010 electron microscope (JEOL, Japan) with an acceleration voltage of 300 kV. The crystalline structures of the samples were evaluated by X-ray diffraction (XRD) analysis on a Bruker D8 Advance Diffractometer with Cu Kα radiation (λ = 1.5418 Å).

2.3. Sorption studies

Adsorption kinetic study: 10 mg of MnO_2−CMR was added to 50 mL of 10 mg L^{-1} MB aqueous solution. The mixture was shaken in constant-temperature shaker (ZD-85, ChangZhouGuoHua) for 1 h. The adsorbent used in different temperature (25, 35, 45℃) was labeled with MnO_2−CMR-25, MnO_2−CMR-35, and MnO_2−CMR-45, respectively. After adsorption equilibration, the adsorbent was separated from solution by external magnet. MB concentration after adsorption was measured by visible spectrophotometer (Model 721) at its maximum adsorption wavelength. The amount of MB adsorbed per unit mass of adsorbent was calculated from the following equation:

$$q = \frac{(C_0 - C_e)V}{m} \quad (1)$$

where C_0 and C_e are the initial and equilibrium concentrations of MB, respectively (mg L^{-1}); q is the

adsorption capacity of adsorbent for MB (mg g^{-1}); V is the volume of MB solution (mL); m is the mass of the dry adsorbent used (mg).

Adsorption isotherm study: 10 mg of MnO_2–CMR was added to 50 mL of MB solution with different initial concentration (10–120 mg L^{-1}), and shaken for 2 h. The equilibration concentration was determined by visible spectrophotometer (Model 721) at 668 nm wavelength. Adsorption data obtained in this experimental study were evaluated with Freundlich and Langmuir isotherms models.

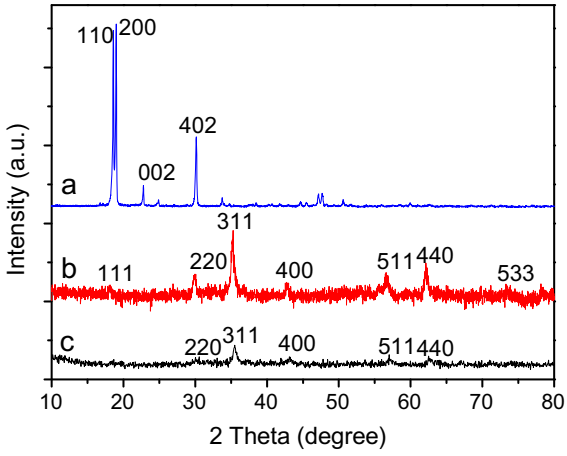

Fig. 1. XRD patterns of the cobalt ferroxalate precursor (a), the calcined sample (b), and the modified samples (c).

3. Results and discussion

3.1. Characterization of the as-prepared samples

XRD patterns of the cobalt ferroxalate precursor, the calcined sample and the modified samples are shown in Fig. 1. In Fig. 1(a), XRD characteristic peaks at $2\theta = 18.69^\circ$, 19.05°, 23.25°, 28.76° are observable, which can be indexed to the oxalate in terms of α-form with monoclinic C2/c [17]. The diffraction peaks of the calcined product as shown in Fig. 1(b) are identical with the cubic spinel phase of $CoFe_2O_4$ (JCPDS-03-0864). The diffraction peaks in the modified sample (Fig. 1(c)) assigned to $CoFe_2O_4$ can also be observed. However, the intensity of the peaks at 38.12°, 44.32°, 65.04°, and 77.16° is lower than that of the calcined products and there was no peak corresponding to

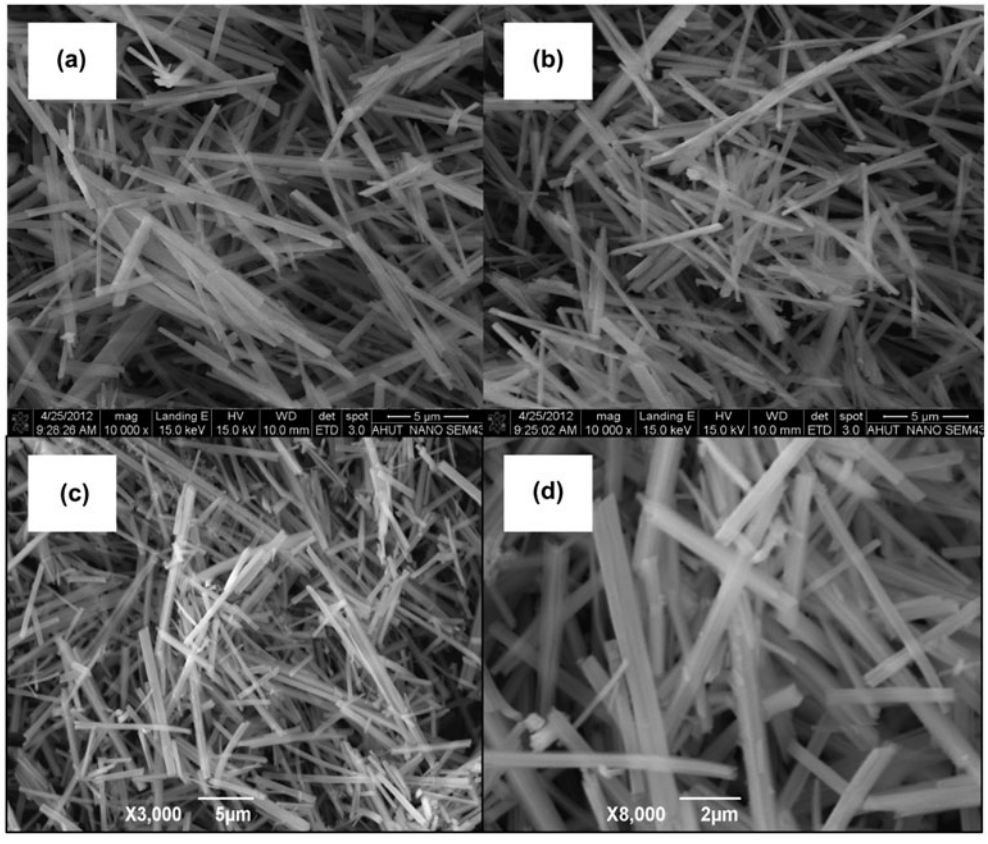

Fig. 2. SEM images of the cobalt ferrioxalate precursor (a), the calcined sample (b), and the modified samples (c and d).

MnO_x, indicating that the produced MnO_x was amorphous in the composite.

Scanning electron microscopy (SEM) images of the cobalt ferrioxalate precursor, the calcined sample, and the modified samples are shown in Fig. 2. It is obvious that calcination did not change the overall morphology of the precursor (Fig. 2(a)). The calcined sample (Fig. 2(b)) through a topotactic reaction well maintained the rod-like morphology of the cobalt ferrioxalate precursor with about 10 μm in length. When the calcined samples were modified by MnO_2, the as-obtained $MnO_2/CoFe_2O_4$ composites also showed rod-like morphology (Fig. 2(c)), magnified SEM image (Fig. 2(d)) shows that the modified samples displayed the rough surface.

In order to further analyze the microstructure of the sample, the as-prepared samples are further characterized by TEM. TEM images of the cobalt ferrioxalate precursor, the calcined sample, and the modified samples are shown in Fig. 3. As shown in Fig. 3(a), cobalt ferrioxalate microrods are stuffed, the surface is smooth, and no pore structure can be found. When the cobalt ferrioxalate microrods are calcined in air, pore structures were produced in the solid rod of the precursor (Fig. 3(b)). The porous structure built by plenty of the as-formed nanoparticles can be clearly seen. The preparation of porous metal oxides through the oxalate precursor had been largely reported by several groups including ours [18–20]. The N2 sorption–desorption isotherms of $CoFe_2O_4$ CMR exhibit IV-type curves as shown in Fig. 3(c). A sharp peak of mesopore size distribution can be observed. The average mesopore size of $CoFe_2O_4$ CMR is 5.2 nm (Fig. 3(c), insets), and its BET surface area and total pore volume are calculated to be 54 $m^2 g^{-1}$ and 0.196 $cm^3 g^{-1}$, respectively.

Magnetic porous materials prepared by this method possess some advantages such as higher surface and rigid texture. Therefore, the as-prepared $CoFe_2O_4$ microrods are employed as a magnetic carrier to apply to the removal of contaminant. A TEM image of $CoFe_2O_4$ microrods modified by MnO_2 is shown in Fig. 3(d). By comparison with the unmodified porous $CoFe_2O_4$ microrods, it can be seen that the pore structure is evidently diminished in the texture even though the rod-like morphology is well

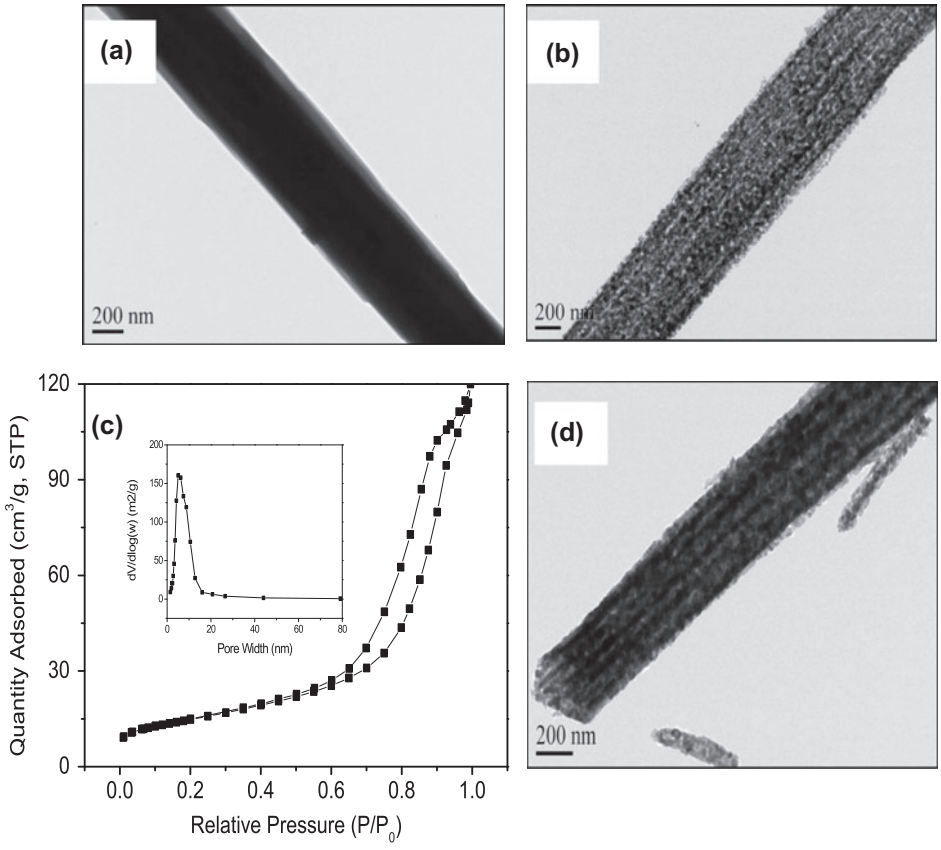

Fig. 3. TTEM images of the cobalt ferrioxalate precursor (a), the calcined sample (b), nitrogen adsorption–desorption isotherms (inset, the pore-size distribution) of the calcined sample (c), and the modified samples (d).

maintained. Manganese oxides were *in situ* formed in the pore structure of the porous $CoFe_2O_4$ microrods. The reaction in the pore can be expressed as follows:

$$2KMnO_4 + 3MnSO_4 + 2H_2O == \\ = 5MnO_2 + 2H_2SO_4 + K_2SO_4 \quad (2)$$

Fig. 4(a) shows energy dispersive spectrometer (EDS) analysis of the modified samples. The existence of Mn, Co, Fe, and O were detected. The ratio of Co and Fe is determined to be 1:2. However, the ratio of Mn and Fe is about 0.01:1, indicating the content of MnO_2 in the composite is much lower than that of $CoFe_2O_4$. Combining the results of XRD, SEM, and TEM results, we confirm that MnO_2 was successfully implanted into the porous texture of $CoFe_2O_4$ microrods. The formation process of the $MnO_2/CoFe_2O_4$ microrods was graphically described by Fig. 4(b). Cobalt ferrioxalate microrods by solvothermal method converted into porous $CoFe_2O_4$ microrods built by nanoparticles. Mn^{2+} can effectively be adsorbed into the porous structure during the soaking process. MnO_2 can be produced by *in situ* reaction in the pore due to the strong oxidation of $KMnO_4$. It should be pointed out that the concentration of $KMnO_4$ is a key for the conservation of the original morphology, and too high concentration (>6 M) of $KMnO_4$ would result in the complete disassembly of the rod-like morphology due to the growth of MnO_2 in the pore of $CoFe_2O_4$ rods (Fig. S1).

3.2. Adsorption properties of MnO_2-modified $CoFe_2O_4$ microrods (MnO_2−CMR)

3.2.1. Adsorption kinetic of MnO_2−CMR for MB

The adsorption kinetics of MB on MnO_2–CMR was studied to investigate the adsorption rate. Fig. 5 shows the effect of the contact time on the adsorption capacities of CMR and MnO_2−CMR for MB under the condition of different temperature. No obvious adsorption

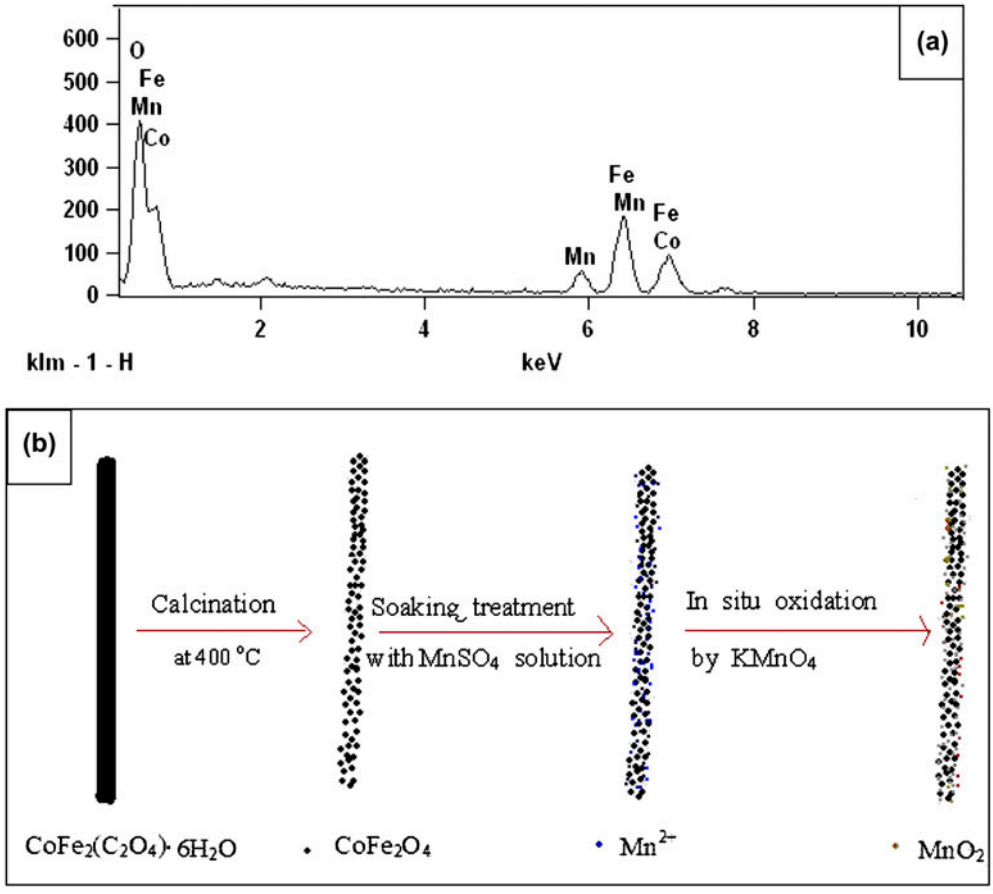

Fig. 4. EDS pattern (a) and schematic illustration for the formation processes and (b) of MnO_2-modified $CoFe_2O_4$ microrods (m-CMR).

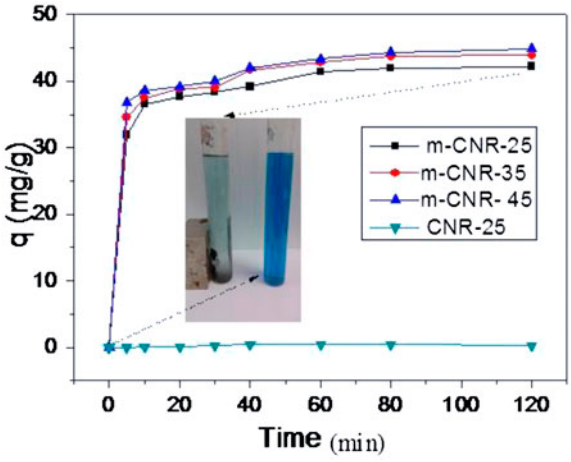

Fig. 5. Adsorbed amount of MB by CMR and m-CMR as a function of contact time at 25, 35, and 45°C, respectively.

can be determined using CMR as adsorbent (CMR-25), and MnO_2–CMR displays excellent adsorption for MB (MnO_2–CMR-25), which indicated that the *in situ* formed MnO_2 was responsible for the enhanced adsorption capacity. The manganese dioxide nanomaterials (in nearly neutral solutions with a pH of 7.0) had abundant hydroxyl groups on the surface [21]. Rich hydroxyl groups on the surface of the newly formed MnO_2 supplied plenty of active site for adsorption. The surface hydroxyl groups and cationic groups of MB have strong electrostatic attraction. Moreover, hydrogen bonding interaction happens between nitrogen atoms in the molecular structure of MB and the surface hydroxyl groups of MnO_2. These led to the better adsorption ability of MnO_2–CMR. Using MnO_2–CMR as adsorbent, the variation tendency of the adsorption curve with time in various adsorption temperatures was shown in Fig. 5. At the initial stage, the adsorption capacity rapidly increased. With the increasing adsorption time, the adsorption capacity slowly increased and the adsorption equilibrium could be achieved within 40 min. At least 80% of MB can be removed from the simulated wastewater. Moreover, the adsorption capacity slightly increased with the increasing adsorption temperature. The as-prepared MnO_2–CMR can be collected easily from the wastewater by an external magnetic field (inset).

The commonly used pseudo-first-order (Eq. (3)) and pseudo-second-order models (Eq. (4)) were employed to examine the controlling mechanism of the adsorption process [22]. The above-mentioned models are expressed as follows:

$$\ln(q_e - q_t) = \ln(q_e) - k_1 t \tag{3}$$

$$\frac{t}{q_t} = \frac{1}{k_2 q_e^2} + \frac{t}{q_e} \tag{4}$$

where q_e (mg g^{-1}) and q_t (mg g^{-1}) are the adsorption capacity at equilibrium and any time t (min), k_1(min^{-1}), and k_2 (g mg^{-1} min^{-1}) are the kinetics rate constants for the pseudo-first-order and pseudo-second-order models, respectively. The kinetic curves fitted according to the two models are shown in Fig. 6(a) and (b). The kinetic constants obtained by linear regression for the two models are summarized in Table 1. Correlation coefficients R^2 values for pseudo-second-order model can reach up to 0.99 and are greater than that of the pseudo-first-order kinetic model. Furthermore, the calculated adsorption equilibrium capacity by pseudo-second-order model agrees well with the experimental data. Therefore, the

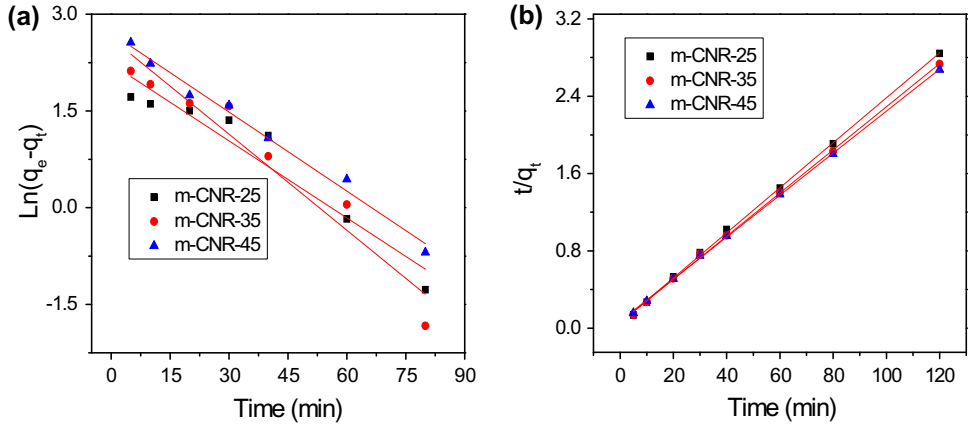

Fig. 6. Kinetics of MB adsorption on m-CMR at 25, 35, and 45°C: (a) pseudo-first-order plot and (b) pseudo-second-order plot.

Table 1
Kinetic models for MB adsorption onto m-CMR

Temperature (℃)	Pseudo-first-order			Pseudo-second-order		
	k_1	q_e	R^2	k_2	q_e	R^2
25	0.0398	9.9299	0.9072	0.0101	42.9001	0.9992
35	0.0496	13.8510	0.9252	0.0085	44.7828	0.9993
45	0.0508	14.9707	0.9855	0.0096	45.9882	0.9996

adsorption process of MnO_2−CMR for MB can be described by pseudo-second-order model.

3.2.2. Adsorption isotherms of MnO_2−CMR for MB

The interaction of the pollutant with sorbent materials can be described by adsorption isotherms, which guide the design of adsorption systems. The isotherms of MB on MnO_2−CMR at 25, 35, and 45℃ are shown in Fig. 7(a), which relate the equilibrium adsorption capacity to the equilibrium concentration in the solution. The Langmuir isotherm model and Freundlich isotherm model were employed to investigate the adsorption process [23]. The two isotherm equations can be expressed as follows:

$$\ln(q_e) = \ln(K_F) + \frac{1}{n}\ln(C_e) \tag{5}$$

$$\frac{C_e}{q_e} = \frac{1}{q_m K_L} + \frac{1}{q_m} C_e \tag{6}$$

$$R_L = \frac{1}{1 + K_L C_0} \tag{7}$$

where q_e and C_e are the adsorption capacity and concentration (mg g^{-1}) at the adsorption equilibrium, q_m is the maximum adsorption capacity (mg g^{-1}), K_L (L mg^{-1}) is the Langmuir equilibrium constant and

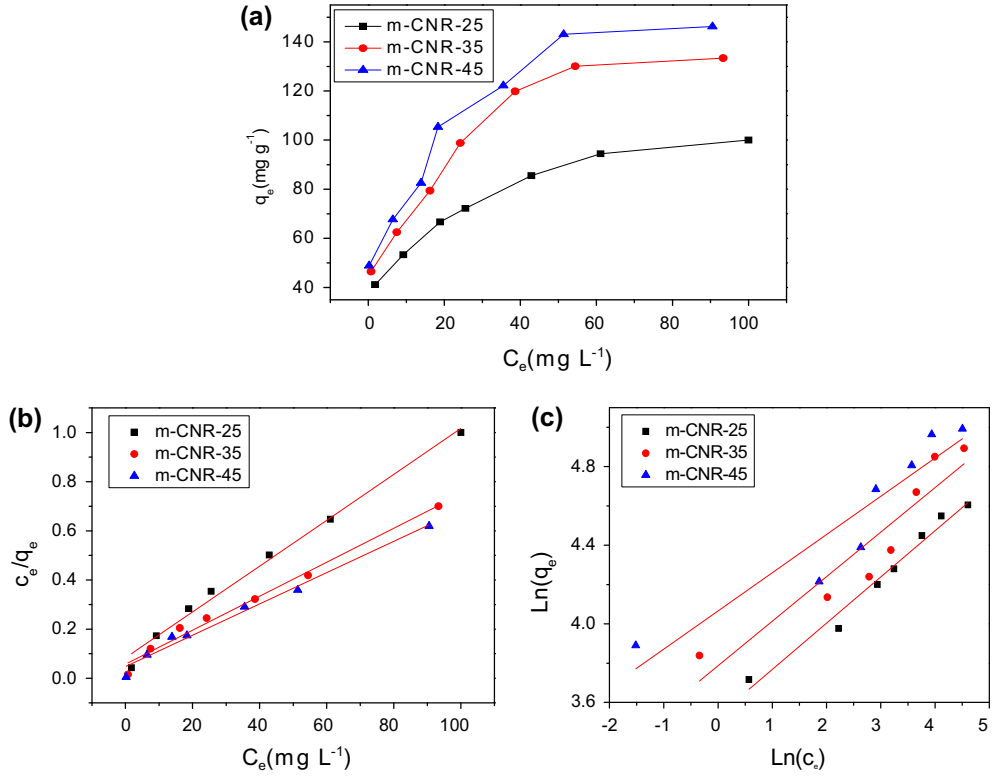

Fig. 7. Adsorption isotherms for MB on m-CMR (a), Langmuir isotherm (b), and Freundlich isotherm (c) at 25, 35, and 45℃, respectively.

can be calculated from the intercepts and the slopes of the linear plots of C_e/q_e vs. C_e. K_F (L g^{-1}) is the Freundlich equilibrium constant and n is the dimensionless exponent of the MB on MnO_2−CMR. The values of K_F and $1/n$ are obtained from the linear plots of ln q_e vs. ln C_e. The plots of C_e/q_e vs. C_e and ln q_e vs. ln C_e are shown in Fig. 7(b) and (c), respectively. Table 2 summarizes the Langmuir and Freundlich adsorption constants and the calculated regression coefficients (R^2). The Langmuir isotherm has higher R^2 values ($R^2 > 0.98$) than did the Freundlich isotherm, indicating the monomolecular adsorption yields a better fit for the experimental equilibrium adsorption data. The maximum adsorption capacities are 107.18, 144.71, and 156.99 mg g^{-1} at the adsorption temperature of 25, 35, and 45°C, respectively. The adsorption capacity of the as-prepared MnO_2−CMR and other adsorbents for MB are compared and presented in Table 3. Comparable or higher adsorption capacity for MB indicate that MnO_2−CMR be employed as an excellent adsorbent. The feasibility of adsorption on adsorbent was evaluated by dimensionless constant separation factor (R_L), which is considered as a more reliable indicator of the adsorption. The value of R_L indicates that the adsorption process on sorbent materials is unfavorable ($R_L > 1$), linear ($R_L = 1$), favorable ($0 < R_L < 1$), or irreversible ($R_L = 0$) [24]. The calculated R_L values are in the range of 0.028–0.17, suggesting MB adsorption onto the MnO_2−CMR is favorable.

3.2.3. Thermodynamic analyses

The thermodynamic parameters such as standard Gibbs free energy change (ΔG°, kJ mol^{-1}), standard enthalpy change (ΔH°, kJ mol^{-1}) and standard entropy change (ΔS°, J mol K^{-1}) can be calculated from the following equation:

$$\Delta G^\circ = -RT \ln K^\circ$$

$$\ln K^\circ = \frac{\Delta S^\circ}{R} - \frac{\Delta H^\circ}{RT}$$

Table 2
Isotherm parameters for MB adsorption onto m-CMR

	Langmuir constants				Freundlich constants		
Temperature (°C)	q_m (mg g^{-1})	K_L (L mg^{-1})	R^2	R_L	K_F (mg g^{-1})	n (L mg^{-1})	R^2
25	107.18	0.1126	0.9895	0.0689–0.4703	34.2189	4.2513	0.9750
35	144.71	0.1206	0.9832	0.0646–0.4533	45.7201	4.4192	0.9160
45	156.99	0.1336	0.9819	0.0587–0.4281	58.3400	5.1688	0.8704

Table 3
Comparison of maximum adsorption capacities for MB on different adsorbents at the condition of 25°C

Adsorbent	Adsorbate	Adsorption capacity (mg g^{-1})	Refs.
Magnetic graphene-carbon nanotube	Methylene blue	65.79	[25]
Poly(cyclotriphosphazene-co-4,4-sulfonyldiphenol) nanotubes	Methylene blue	69.16	[26]
Humic acid-coated Fe_3O_4 nanoparticles	Methylene blue	93.08	[27]
Porous $Mn_{1-x}Zn_xFe_2O_4$ ($0 < x < 0.8$)	Methylene Blue	40.9668	[28]
Titanate nanotubes	Methylene blue	133.33	[29]
Cu-BTC	Methylene blue	4.875	[30]
3D flower-like hierarchical Fe_3O_4/K_xMnO_2 core–shell architectures	Methylene blue	25.64	[31]
m-CNR	Methylene blue	107.18	Present work

Table 4
Thermodynamic data for the adsorption of MB on m-CMR

Temperature (°C)	ΔG° (kJ mol^{-1})	ΔH° (kJ mol^{-1})	ΔS° (J mol^{-1} K^{-1})
25	−35.96	6.726	143.13
35	−37.37		
45	−38.83		

where R is the gas constant, K° is the equilibrium constant (obtained from Langmuir equation), and T is the temperature (K). The values of ΔH° and ΔS° can be calculated from the slope and the intercept of a linear plot of ln K° against 1/T. The value of ΔG°, ΔH°, and ΔS° are presented in Table 4. The negative values of ΔG° show the spontaneity of adsorption. The absolute value of ΔG° increased with the increasing adsorption temperature, indicating the driving force of adsorption is greater at higher temperature. The positive values of ΔH° confirms the endothermic nature of the adsorption process, and the values of ΔH° is lower than 40 kJ mol^{-1}, indicating physisorption is dominant for the adsorption of MB onto MnO_2−CMR. The positive ΔS° means the increase of freedom degrees at the adsorbent–adsorbate interface during the adsorption process.

4. Conclusion

In summary, MnO_2–CMR was successfully prepared by *in situ* modification of MnO_2 in the texture of CMR through the reaction of the adsorbed Mn^{2+} and $KMnO_4$. The adsorptive property of the as-prepared MnO_2–CMR was investigated in detail. The as-prepared MnO_2−CMR exhibited better adsorption properties for MB than did CMR. The experimental data of MB adsorption suggested that the pseudo-second-order kinetic model was suitable for explaining the adsorption kinetic process with better correlation coefficients than pseudo-first-order kinetic model, and Langmuir model fits the adsorption of MB better than did the Freundlich model. The adsorption thermodynamics showed that the adsorption was a spontaneous and endothermal process. In addition, the as-prepared material as sorbent can be magnetically recycled by a magnet. This study may provide a new approach for the aggregation of magnetic nanoparticles with important application in wastewater.

Supplementary material

The supplementary material for this paper is available online at http://dx.doi.10.1080/19443994.2015.1099473.

Acknowledgments

This work is supported by National Natural Science Foundation of China (20907001), Training Programs of Innovation for Undergraduates of Anhui Province (AH201310360150, AH201310360279), Student Research Training Program of AHUT (2013034Y), and Outstanding Innovation Team of Anhui University of Technology (TD201202).

References

[1] P. Kumar, R. Agnihotri, K.L. Wasewar, H. Uslu, C.K. Yoo, Status of adsorptive removal of dye from textile industry effluent, Desalin. Water Treat. 50 (2012) 226–244.
[2] Z. Yang, H. Yang, Z.W. Jiang, T. Cai, H.J. Li, H.B. Li, A.M. Li, R.S. Cheng, Flocculation of both anionic and cationic dyes in aqueous solutions by the amphoteric grafting flocculant carboxymethyl chitosan-graft-polyacrylamide, J. Hazard. Mater. 254–255 (2013) 36–45.
[3] X. Huang, X.W. Bo, Y.X. Zhao, B.Y. Gao, Y. Wang, S.L. Sun, Q.Y. Yue, Q. Li, Effects of compound bioflocculant on coagulation performance and floc properties for dye removal, Bioresour. Technol. 165 (2014) 116–121.
[4] X.M. Peng, D.P. Huang, T. Odoom-Wubah, D.F. Fu, J.L. Huang, Q.D. Qin, Adsorption of anionic and cationic dyes on ferromagnetic ordered mesoporous carbon from aqueous solution: Equilibrium, thermodynamic and kinetics, J. Colloid Interface Sci. 430 (2014) 272–282.
[5] C. Xu, A.J. Cui, Y.L. Xu, X.Z. Fu, Graphene oxide–TiO_2 composite filtration membranes and their potential application for water purification, Carbon 62 (2013) 465–471.
[6] S. Senthilkumar, C. Basha, M. Perumalsamy, H.J. Prabhu, Electrochemical oxidation and aerobic biodegradation with isolated bacterial strains for dye wastewater: Combined and integrated approach, Electrochim. Acta 77 (2012) 171–178.
[7] F. Ferella, I. De Michelis, C. Zerbini, F. Vegliò, Advanced treatment of industrial wastewater by membrane filtration and ozonization, Desalination 313 (2013) 1–11.
[8] H.G. Li, Y.W. Lin, Y.B. Luo, P. Yu, L.W. Hou, Relating organic fouling of reverse osmosis membranes to adsorption during the reclamation of secondary effluents containing methylene blue and rhodamine B, J. Hazard. Mater. 192 (2011) 490–499.
[9] Y.Y. Yao, L. Wang, L.J. Sun, S. Zhu, Z.F. Huang, Y.J. Mao, W.Y. Lu, W.X. Chen, Efficient removal of

dyes using heterogeneous Fenton catalysts based on activated carbon fibers with enhanced activity, Chem. Eng. Sci. 101 (2013) 424–431.
[10] F. Torrades, J. García-Montaño, Using central composite experimental design to optimize the degradation of real dye wastewater by Fenton and photo-Fenton reactions, Dyes Pigm. 100 (2014) 184–189.
[11] G.Z. Kyzas, E.A. Deliyanni, N.K. Lazaridis, Magnetic modification of microporous carbon for dye adsorption, J. Colloid Interface Sci. 430 (2014) 166–173.
[12] W. Konicki, D. Sibera, E. Mijowska, Z. Lendzion-Bieluń, U. Narkiewicz, Equilibrium and kinetic studies on acid dye Acid Red 88 adsorption by magnetic $ZnFe_2O_4$ spinel ferrite nanoparticles, J. Colloid Interface Sci. 398 (2013) 152–160.
[13] R.R. Shan, L.G. Yan, K. Yang, S.J. Yu, Y.F. Hao, H.Q. Yu, B. Du, Magnetic Fe_3O_4/MgAl-LDH composite for effective removal of three red dyes from aqueous solution, Chem. Eng. J. 252 (2014) 38–46.
[14] J. Hu, I.M.C. Lo, G.H. Chen, Fast removal and recovery of Cr(VI) using surface-modified jacobsite ($MnFe_2O_4$) nanoparticles, Langmuir 21 (2005) 11173–11179.
[15] M. Ozaki, H. Suzuki, K. Takahashi, E. Matijević, Reversible ordered agglomeration of hematite particles due to weak magnetic interactions, J. Colloid Interface Sci. 113 (1986) 76–80.
[16] Z.G. Jia, D.P. Ren, R.S. Zhu, Synthesis, characterization and magnetic properties of $CoFe_2O_4$ nanorods, Mater. Lett. 66 (2012) 128–131.
[17] Y.U. Park, J. Kim, H. Gwon, D.H. Seo, S.W. Kim, K. Kang, Synthesis of multicomponent olivine by a Novel mixed transition metal oxalate coprecipitation method and electrochemical characterization, Chem. Mater. 22 (2010) 2573–2581.
[18] L.M. Guo, H. Arafune, N. Teramae, Synthesis of mesoporous metal oxide by the thermal decomposition of oxalate precursor, Langmuir 29 (2013) 4404–4412.
[19] Z.G. Jia, D.P. Ren, L.X. Xu, Generalized preparation of metal oxalate nano/submicro-rods by facile solvothermal method and their calcined products, Mater. Lett. 76 (2012) 194–197.
[20] L.H. Ai, H.T. Yue, J. Jiang, Sacrificial template-directed synthesis of mesoporous manganese oxide architectures with superior performance for organic dye adsorption, Nanoscale 4 (2012) 5401–5408.
[21] H.M. Chen, P.K. Chu, J.H. He, T. Hu, M.Q. Yang, Porous magnetic manganese oxide nanostructures: Synthesis and their application in water treatment, J. Colloid Interface Sci. 359 (2011) 68–74.
[22] L.P. Wang, Z.C. Huang, M.Y. Zhang, B. Chai, Adsorption of methylene blue from aqueous solution on modified ACFs by chemical vapor deposition, Chem. Eng. J. 189–190 (2012) 168–174.
[23] C. Kannan, K. Muthuraja, M.R. Devi, Hazardous dyes removal from aqueous solution over mesoporous aluminophosphate with textural porosity by adsorption, J. Hazard. Mater. 244–245 (2013) 10–20.
[24] S. Vasiliu, I. Bunia, S. Racovita, V. Neagu, Adsorption of cefotaxime sodium salt on polymer coated ion exchange resin microparticles: Kinetics, equilibrium and thermodynamic studies, Carbohydr. Polym. 85 (2011) 376–387.
[25] P.F. Wang, M.H. Cao, C. Wang, Y.H. Ao, J. Hou, J. Qian, Kinetics and thermodynamics of adsorption of methylene blue by a magnetic graphene-carbon nanotube composite, Appl. Surf. Sci. 290 (2014) 116–124.
[26] Z.H. Chen, J.N. Zhang, J.W. Fu, M.H. Wang, X.Z. Wang, R.P. Han, Q. Xu, Adsorption of methylene blue onto poly(cyclotriphosphazene-co-4,4´-sulfonyldiphenol) nanotubes: Kinetics, isotherm and thermodynamics analysis, J. Hazard. Mater. 273 (2014) 263–271.
[27] X. Zhang, P.Y. Zhang, Z. Wu, L. Zhang, G.M. Zeng, C.J. Zhou, Adsorption of methylene blue onto humic acid-coated Fe_3O_4 nanoparticles, Colloids Surf., A 435 (2013) 85–90.
[28] X.Y. Hou, J. Feng, X.H. Liu, Y.M. Ren, Z.J. Fan, M.L. Zhang, Magnetic and high rate adsorption properties of porous $Mn_{1-x}Zn_xFe_2O_4$ ($0 \le x \le 0.8$) adsorbents, J. Colloid Interface Sci. 353 (2011) 524–529 .
[29] L. Xiong, Y. Yang, J.X. Mai, W.L. Sun, C.Y. Zhang, D.P. Wei, Q. Chen, J.R. Ni, Adsorption behavior of methylene blue onto titanate nanotubes, Chem. Eng. J. 156 (2010) 313–320.
[30] S. Lin, Z.L. Song, G.B. Che, A. Ren, P. Li, C.B. Liu, J.S. Zhang, Adsorption behavior of metal–organic frameworks for methylene blue from aqueous solution, Microporous Mesoporous Mater. 193 (2014) 27–34.
[31] X.Y. Li, S.Y. Song, X. Wang, D.P. Liu, H.J. Zhang, Self-assembled 3D flower-like hierarchical Fe_3O_4/K_xMnO_2 core–shell architectures and their application for removal of dye pollutants, CrystEngComm. 14 (2012) 2866–2870.